

# Theoretical Modeling of Levitated Clusters of Water Droplets Stabilized by Infrared Irradiation

M. Q. Brewster

Department of Mechanical Science and Engineering, University of Illinois at Urbana-Champaign, Urbana, IL 61801 e-mail: brewster@illinois.edu

This paper shows how clusters of radiation-stabilized water droplets levitated in an upward flow of air and water vapor above a heated water surface can be modeled using Spalding's self-similarity theory of heat and mass transfer and Stefan flow. The model describes equilibrium droplet states, including stability conditions, as well as nonequilibrium (quasi-steady) transient evolution. Equilibrium states are shown to exist when Stefan-flow supersaturation, which has a quadratic-like variation with height above the water surface, and radiation-stabilized equilibrium supersaturation, which is nearly constant with height, are equal. The latter can be predicted by a fundamentally derived function of absorbed radiant flux (linear), droplet radius (linear if opaque), continuum thermal conductivity, and thermodynamic properties. In fact, all of the experimentally observed droplet behavior can be predicted using simple analytical results based on quasi-steady droplet energy and continuum transport. Unsteady droplet energy, Knudsen-layer transport, numerical solutions, and curve-fitting of numerical computations, as used previously in modeling this behavior, are not necessary. An interesting reversal of the usual effect of mass transfer on droplet drag in low-Re flow when levitated droplets are irradiated asymmetrically by significant infrared radiation is also postulated, which relates to the relative importance of normal (pressure) and tangential (shear stress) drag. This theory of radiation-augmented droplet evaporation, condensation, and relative motion in a moving gas has application to conditions in clouds, wherein droplets can experience either net radiative heating or cooling and fluctuating updrafts or downdrafts. [DOI: 10.1115/1.4053415]

#### 1 Introduction

Radiation stabilization of mist-size water droplets that would otherwise grow by condensation in a supersaturated environment is an interesting heat-mass-transfer phenomenon that has been predicted theoretically and recently verified experimentally [1–3]. Theoretical prediction of the stabilizing effect of radiation was first reported in 2015 [2] with experimental verification following in 2020 [1]. The experimental work [1] demonstrated that mistsize spherical water droplets can be levitated as stable, monosized cluster arrays above a water surface under the influence of infrared radiation. In addition to these equilibrium states of no droplet growth or shrinkage that occurred with a certain level of irradiation flux, condensational growth and evaporative shrinkage were also demonstrated to occur at a lower level of radiant flux. In addition to the experimental demonstration of radiation stabilization and the reporting of new laboratory measurements of equilibrium droplet size and transient droplet-size evolution-all of which are significant accomplishments-modeling results were also reported based on unsteady numerical analysis [1]. The latter modeling results, however, ignored previously published findings about modeling droplet heat- and mass-transfer under the influence of radiation [2,3]. This paper shows how that unsteady numerical modeling could have been done more simply using previously published quasi-steady analytical theory [2,3] and how the equilibrium levitated states, including their stability conditions, can be modeled using a simple Stefan-flow model coupled with previously published heat- and mass-transfer theory based on the selfsimilar Spalding model [4]. This paper also demonstrates how continuum (Fick's law) diffusion-mass-transfer is applicable

Contributed by the Heat Transfer Division of ASME for publication in the JOURNAL OF HEAT TRANSFER. Manuscript received May 27, 2021; final manuscript received December 28, 2021; published online March 1, 2022. Assoc. Editor: Milind A. Log.

under the considered conditions and that more complicated, noncontinuum, Knudsen-layer modeling [1] is not necessary. This paper also postulates an interesting possible reversal of the usual effect of mass transfer on droplet drag in low-Re flow when levitated droplets are irradiated asymmetrically. All of this has application to conditions inside clouds, which are arguably the least understood, i.e., least predictable, planetary thermal regulating substance in Earth's atmosphere.

The laboratory experiment of Ref. [1] (see Fig. 1) uses both broadband infrared radiation (1-20 μm, blackbody temperature 1223 K) with flux q obliquely incident from above the horizontal array of droplets and near-infrared (0.808  $\mu$ m) laser radiation with flux  $q_o$  normally incident from below. There are two stabilizing aspects to this radiation-assisted technique. The first has to do with the droplets being levitated in a supersaturated upward flow of water vapor (and air) from a thin (400  $\mu$ m), horizontal liquid water layer, from whence the vapor for the droplets originates. The upward water-vapor flow is generated by absorption of the laser radiation by a blackened glass substrate that supports the water layer. This first (hydrodynamic) stabilizing effect is not peculiar to radiation and could be accomplished by any source of heat into the water layer to generate the upward flow of supersaturated vapor. The second stabilizing aspect is associated with the broadband infrared radiation and is peculiar to direct radiant heating of droplets. This phenomenon has to do with the intriguing stabilizing effect that external incident radiation can have on water droplets that would otherwise grow by condensation in the supersaturated environment.

External radiation absorbed by cloud or mist-sized (5–20  $\mu$ m radius) water droplets creates a positive slope in the droplets' theoretical Kohler–Kelvin curves, as pointed out in Ref. [2], which means that the droplets are intrinsically stable in ambient environments with relatively fixed supersaturation (unlike points on negative-slope branches of the curves). That is, droplets that

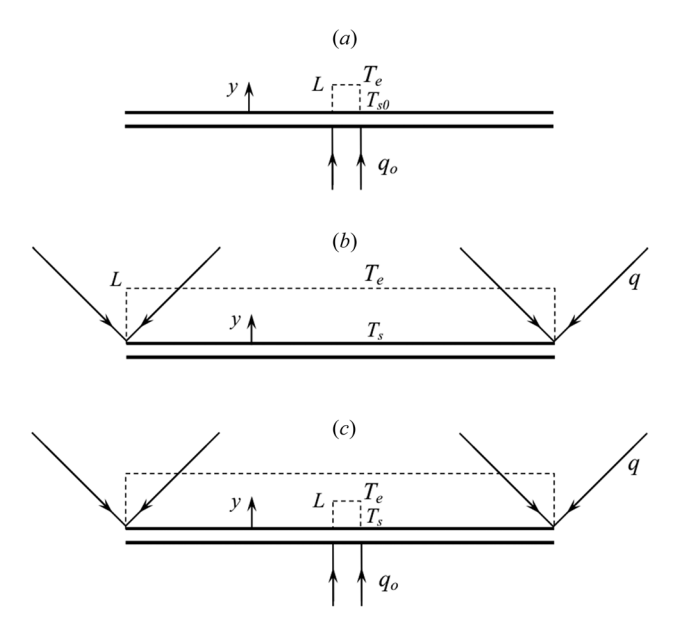


Fig. 1 Schematic diagram of water film on glass substrate being heated by: (a) only laser irradiation with flux  $q_o$  from below, (b) only broadband infrared irradiation with flux q from above, and (c) both laser from below and broadband-infrared from above

are formed or appear in a slightly supersaturated environment can persist at constant size and constant temperature when they are irradiated by radiation of which they are efficient absorbers and thus raised in temperature slightly above the surrounding vapor such that the absorbed radiant energy balances the energy conducted away from the droplet to the vapor. In this equilibrium condition, the evaporative mass flux that would have been generated by the absorbed radiation (i.e., "virtual" evaporative flux) balances the condensative mass flux that would have been generated by the supersaturated condition of the surrounding vapor (i.e., virtual condensative flux), resulting in no net evaporation or condensation of water and thus no droplet growth or shrinkage. The mathematical theory that describes this phenomenon was previously addressed in Refs. [2] and [3]. However, Ref. [1] did not point this out. Rather, it simply grouped [2,3] with four other papers (Refs. [25], [26], [29], and [30] in Ref. [1]) and noted that, 'a similar effect of thermal radiation on size of water droplets takes place in the atmosphere and in diverse engineering problems." That is, with respect to acknowledging Refs. [2] and [3], the text only made reference to "important differences" between how clouds are formed versus how the levitated droplets are formed and how infrared radiation in clouds is more diffuse versus the more semicollimated infrared irradiation in the levitated droplet experiments. Such differences are actually rather insignificant. The analytical theory described in Ref. [2] did not restrict the incident radiation to being diffuse. The theory in Ref. [2] applies as well to the laboratory-levitated, radiation-stabilized droplets as it does to more naturally formed mists and clouds. The assertion in Ref. [1] that, "Obviously, the effect of external infrared heating of a droplet cluster is quite another physical problem that [sic] those considered in studies of atmospheric mists or clouds," is simply not true.

Table 1 Experimental equilibrium properties of levitated droplets from Ref. [1]

			1	2	3	4	5	6	7
2 3 4	$a_{\rm eq} (\mu \rm m)$	T1 <sup>a</sup> T1, S5.3 F4, T1, S5.3 F4	5.5	47.3 9.4 9.0	9.95	57.6 10.85 8.25	61.2 11.4	66.7 13.5 6.0	69.3

<sup>a</sup>Source of data: T1 = Table 1 [1]; F4 = Fig. 4 [1]; S5.3 = Sec. 5.3 [1]; and row 5 is calculated from  $T_s$  data of T1 (row 2) and  $\Delta T_s/T_{s0}$  data of F4 (row 4) by  $T_{s0} = T_s/(1 + \Delta T_s/T_{s0})$ .

## 2 Equilibrium (Steady) Conditions

When a water layer in air is heated from below (for example, by laser radiation [1]), droplets a few tens of microns in radius are formed within several tens of microns of the water layer surface by heterogeneous condensation on airborne cloud-condensation nuclei (CCN) in the supersaturated vapor above the water surface. These droplets are partially suspended above the water layer by the upward flow of vapor (water and air). Without any direct irradiation of the droplets from above, the droplets undergo transient evolution, condensative growth, until they become large enough to fall by gravity into the water layer. If broadband infrared irradiation is introduced from above onto the partially suspended, transient droplet array, this transient evolution can proceed toward an equilibrium steady-state characterized by a uniform droplet radius,  $a_{eq}$ , with smaller droplets ( $a < a_{eq}$ ) continuing to grow by condensation toward  $a_{\rm eq}$  and larger droplets  $(a>a_{\rm eq})$  shrinking by evaporation toward  $a_{\rm eq}$ . This equilibrium state depends on the magnitudes of the radiant fluxes. Even the existence of equilibrium states depends on the magnitudes of the radiant fluxes. There is a stability boundary distinguishing conditions that allow equilibrium states from those that do not allow equilibrium states that is determined by the magnitudes of the two radiant fluxes in the experiment, broadband-infrared and laser. First, consider equilibrium conditions and properties, particularly droplet radius, for the locus of points or states that define this stability boundary.

Table 1 shows experimentally determined properties of equilibrium states that are on or near the hydrodynamic stability boundary as obtained from Fig. 4 [1] and Table 1 [1]. In Table 1 rows 1–3 and columns 2–6, experimental values for broadband flux q, water surface temperature  $T_s$ , and droplet radius  $a_{\rm eq}$  are taken from Table 1 [1]. These data appear to be for the same experiments as the data reported in Fig. 4 [1], as revealed by examination of the data for  $a_{\rm eq}$ . The five leftmost data points in Fig. 4(b) [1] are the same as the five data points in Fig. 4(a) [1], as revealed by examination of the data for the fractional change in water surface temperature  $\Delta T_s/T_{s0}$ , which is explained next.

The stability boundary is determined experimentally through variations in infrared flux q ( $\sim$ 3–6 mW/mm² (kW/m²)), and laser flux³ that result in variations in the liquid water surface temperature  $T_s$  that are of the order of tens of ° C. When only laser heating from below is present (Fig. 1(a)), the surface temperature is designated as  $T_{s0}$ ; when both laser heating from below and broadband infrared heating from above are present (Fig. 1(c)), the surface temperature is designated as  $T_s$ . The increase in surface temperature with the addition of the broadband infrared flux is

<sup>&</sup>lt;sup>1</sup>Reference [2] considered water droplets of various sizes, both in the unsteady droplet-energy and quasi-steady droplet-energy regimes. The analysis that would be relevant to Ref. [1] happened to be presented in a section in Ref. [2] that focused on the application of the quasi-steady theory to cloud droplets. A detailed example calculation of unsteady, mm-size laboratory droplet evaporation induced by collimated CO<sub>2</sub> laser radiation was also presented in Refs. [2] and [3].

<sup>&</sup>lt;sup>2</sup>In citing figures, tables, and equations from reference papers, e.g., Ref. [1] or [2], the original numbers are used, with the reference paper number, e.g., Ref. [1] or [2], appended. When no reference paper number appears, that indicates a figure, table, or equation original to this paper.

<sup>&</sup>lt;sup>3</sup>No values are given in Ref. [1] for the laser flux, only a maximum power rating of 800 mW and beam diameter of 1 mm, which corresponds to a maximum spatially averaged flux of 1000 mW/mm<sup>2</sup> (kW/m<sup>2</sup>). It is inferred that the laser flux used was at least an order of magnitude smaller than this maximum flux, probably about 1 order of magnitude larger than the broadband infrared flux.

 $\Delta T_s = (T_s - T_{s0})$  and the fractional increase is  $\Delta T_s/T_{s0}$ , with  $T_{s0}$  given in  $^{\circ}\mathrm{C}.$ 

There is, however, an apparent discrepancy between the water surface temperature data reported in Fig. 4(a) [1] and those reported in Table 1 [1]. Examination of the data for  $T_{s0}$  in Fig. 4(a) [1] and the data for  $T_s$  in Table 1 [1] reveals that the numbers are the same (see also row 2 of Table 1); yet, they should not be (for  $q_o > 0$ ) by their very definitions. Apparently, either the labeling of the horizontal axis of Fig. 4(a) [1] as  $T_{s0}$  is incorrect (should have been  $T_s$ ) or the labeling of  $T_s$  in Table 1 [1] is incorrect (should have been  $T_{s0}$ ). Both of these possibilities were examined and, based on Stefan-flow modeling, it is concluded that the former is the more likely case. Therefore, Table 1 row 2 is labeled consistently with Table 1 [1] as  $T_s$ , and  $T_{s0}$  in row 5 of Table 1 is calculated from this data (not taken from Fig. 4(a) [1]). In row 5 of Table 1, only two values of  $T_{s0}$  are shown, for columns 3 and 6, as these two cases are considered for further modeling below as being representative of a relatively higher flux condition  $(q = 5.58 \text{ kW/m}^2)$  and a relatively lower flux condition  $(q = 3.85 \text{ kW/m}^2)$ , both on, or nearly on, the stability boundary. The case of  $q = 3.01 \text{ kW/m}^2$ , which is an even lower flux than 3.85, is an apparent anomaly, as shown by Fig. 4(b) [1], where the datum point falls below the dashed line that fits the larger set of data describing the stability boundary, and by Fig. 4(a) [1], where that datum point abruptly changes the slope of the stability boundary (i.e.,  $\Delta T_s/T_{s0}$  is unrealistically held constant, at a value of 9%). With this background, it is possible to understand better the data reported in Fig. 4 [1]. Note that no mention has been made yet of the value of laser flux  $q_o$  used during experimental runs, including in Table 1, as these values were not reported in Ref. [1].

Figure 4(a) [1] plots the fractional increase in surface temperature due to broadband infrared heating  $\Delta T_s/T_{s0}$  versus  $T_{s0}$ , and Fig. 4(b) [1] plots the equilibrium droplet radius  $a_{\rm eq}$  versus  $\Delta T_s/T_{s0}$ . Since surface temperature and droplet radius are both dependent variables, this choice of plot variables obscures any clear causeand-effect relationship between changes in a dependent variable that resulted from change in an independent variable. (In Sec. 4, we remedy this situation by replotting Fig. 4 [1].) The text [1] indicates, "...that the ratio  $\Delta T_s/T_{s0}$  shown on the abscissa of Fig. 4(b) is proportional to the infrared radiative flux." This suggests that broadband infrared flux q increases to the right on the horizontal axis of Fig. 4(b) [1]. Detailed examination of the data indicates that actually it is the opposite. The proportionality is actually that just the numerator  $\Delta T_s$  is proportional to broadband infrared flux q for fixed laser flux  $q_o$ , i.e., fixed  $T_{s0}$ . Since two independent variables, i.e., the two independent radiant fluxes, are involved in determining  $\Delta T_s/T_{s0}$ , it is impossible to say how that ratio would vary without specifying the variation in both radiant fluxes. Examination of the experimental data points in Fig. 4 [1] shows that both broadband and laser flux vary such that both the numerator and denominator of  $\Delta T_s/T_{s0}$  vary, and they do so in such a way that infrared flux q actually increases to the left, not to the right, on the horizontal axis of Fig. 4(b) [1], and laser flux  $q_o$  (i.e.,  $T_{s0}$ ) also increases to the left. In Fig. 4(a) [1], laser flux decreases to the left (causing the decrease in  $T_{s0}$ ), and both laser flux and infrared flux decrease going upward on the vertical axis. (For readers that still find the cause-and-effect relationships of Fig. 4 [1] confusing, this issue is revisited and clarified below with model calculations based on Stefan flow.)

Next, consider the equilibrium values of droplet radius, droplet temperature, and surrounding gas supersaturation for states both near and away from the stability boundary, and how these values are determined. At steady-state, the droplet temperature  $T_{\rm eq}$  is slightly higher than the surrounding vapor temperature, as given by the steady droplet energy balance, Eq. (8) [1], or, as explained following Eq. (8) [1], with the gas temperature assumed to be the

same<sup>4</sup> as the measured liquid water surface temperature  $T_s$ , Eq. (9) [1]:

$$T_{\rm eq} = T_s + \frac{a_{\rm eq}Q_a q}{4k} \tag{9}[1]$$

where  $Q_aq$  is the absorbed part of the incident infrared flux q, and k ( $k_{\rm gas}$  in Ref. [1]) is gas thermal conductivity (0.026 W/m K). The factor of 4 in Eq. (9) [1] is the ratio of droplet surface area over which conductive heat flux from the droplet occurs to projected area, over which absorption of semicollimated broadband infrared radiation occurs. Figure 8 [1] shows data for  $T_{\rm eq}$  calculations of five experimental points based on measurements of  $T_s$  and  $a_{\rm eq}$  (and q). The values of  $a_{\rm eq}$  in Fig. 8 [1] indicate that these five data points are the same as the five point of Table 1 [1], i.e., conditions near the hydrodynamic stability boundary, for which,  $T_s$  varied significantly, i.e., over an interval of about 20 °C, because broadband flux q did, from 3.01 to 5.58 kW/m² (and presumably laser flux also varied significantly but this was not reported). Figure 8 [1] also shows corresponding values of gas supersaturation (relative humidity minus one),  $s_{\rm eq} = \varphi_{g,\rm eq} - 1$ , calculated using Eq. (11) [1], where  $P_s$  ( $P_{\rm sat}$  in Ref. [1]) is the saturation pressure

$$\varphi_{g,\text{eq}} = \frac{P_s(T_{\text{eq}})}{P_s(T_s)} \tag{11)[1]}$$

Note that Eq. (11) [1] is not the definition of relative humidity  $\varphi$  but a statement of equality of water-vapor mole or mass fraction between the droplet surface (which is at saturation) and the gas away from the surface at equilibrium. Figure 8 [1] again convolutes dependent and independent variables (or cause and effect), as in Fig. 4 [1], by presenting plots with sets of dependent variables:  $a_{\rm eq}$  or  $T_{\rm eq}$  versus  $s_{\rm eq}$  (Fig. 4(a) [1]) and  $T_{\rm eq}$  versus  $a_{\rm eq}$  (Fig. 4(b) [1]).

Additional results for steady-state properties  $(T_{eq}, s_{eq}, and a_{eq})$ are shown in Fig. 11 [1] for a fixed q value of  $5.58 \,\mathrm{kW/m^2}$ , and for unknown laser flux but with flux magnitudes such that these states are well away from the stability boundary. And, unlike with Fig. 8 [1], the results of Fig. 11 [1] were apparently calculated by numerical solution of unsteady balance equations rather than from steady-state relations. Reference [1] (see caption of Fig. 11 [1]) discusses Fig. 11 [1] in a computational sense, as if  $a_{\rm eq}$  were the independent variable, which, of course, experimentally it could not be. If one tries to imagine how the variations in  $a_{eq}$  in Fig. 11 [1] could come about experimentally for fixed infrared flux q, one could imagine that the variations might be induced by variations in  $T_s$  or  $s_{eq}$ , as might be produced by variations of laser flux. The problem with this physical reasoning is that the text indicates a fixed  $T_s$  value (69.3 °C) for Fig. 11(a) [1], which would require a fixed laser flux. It is thus difficult to know what to think about how the variations in Fig. 11 [1] might be induced physically. Unlike the similar Fig. 8 [1], which can at least be interpreted physically and understood experimentally (as long as it is understood that  $s_{eq}$  is a dependent, not independent, variable, both experimentally and computationally), Fig. 11 [1] seems to be a computational exercise in which both infrared flux and laser flux are fixed (and thus  $T_s$  is fixed) but somehow variations in droplet temperature and supersaturation are induced by independently varying droplet radius. (The conditions of Fig. 11 [1], particularly for  $T_{\rm eq} = 68.9$  °C,  $s_{\rm eq} = 2.56\%$ , and  $a_{\rm eq} = 18.8 \,\mu{\rm m}$ , are considered further below, since they represent the equilibrium state of an initially nonequilibrium cluster used in an illustrative calculation of transient evolution of condensing and evaporating droplets.)

The reason why Fig. 11(a) [1]—hypothetical as it may be physically—was obtained from numerical computations, when it could readily (and accurately) be calculated algebraically using Eq. (9) [1], is not explained in Ref. [1]. The algebraically calculated version of Fig. 11(a) [1] (via Eq. (9) [1]) is shown in Fig. 2(a), and the results are essentially identical to those of Fig. 11(a) [1] except for a small bump near  $a_{eq} = 12 \, \mu m$  in

<sup>&</sup>lt;sup>4</sup>Stefan flow modeling suggests a temperature drop between the water surface and the equilibrium droplet location of several degrees, up to 5 °C for the highest flux case of Table 1 (column 6).

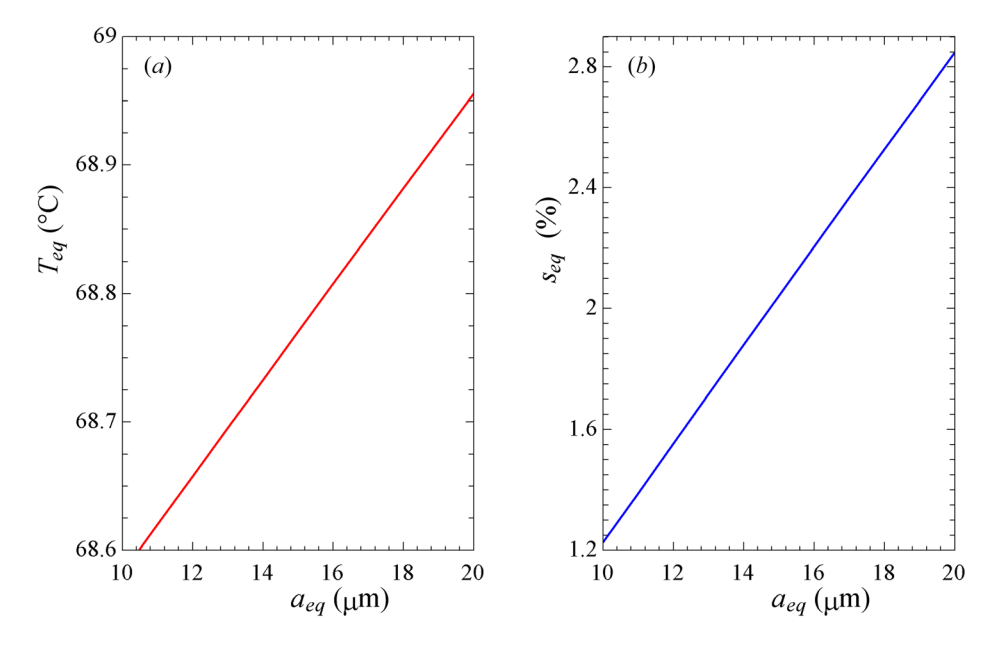


Fig. 2 Equilibrium properties: (a) droplet temperature, (a) and (b) droplet radius, and (b) vapor supersaturation for broadband infrared flux  $q = 5.58 \, \text{kW/m}^2$  and  $T_s = 68.3 \,^{\circ}\text{C}$  corresponding to Fig. 11 [1] but calculated using quasi-steady droplet Eqs. (9) [1] and (61) [2]

Fig. 11(a) [1], which is probably an artifact of the numerical computation of such a finely varying quantity. Figure 2(a) is based on an assumed constant  $T_s$  value of 68.3 °C. As noted above, the text [1] indicates a  $T_s$  value of 69.3 °C for Fig. 11(a) [1], but this value could not be correct for a gas temperature (assuming that  $T_s$  still means gas temperature and not the slightly higher water layer surface temperature) since under infrared irradiation droplet temperature must exceed the gas temperature (if only slightly). And like with Fig. 11(a) [1], in the development and discussion of Fig. 2(a), it seems contradictory both to fix the value of  $T_s$  and to imagine it to vary (via laser flux variation) in order to understand why or how experimentally these properties might vary; however, fixing  $T_s$  and q and independently varying  $a_{eq}$  is apparently what was done in generating Fig. 11 [1] so Fig. 2 has simply followed suit for the sake of consistency in comparing calculated results. Figure 11(b) [1] for  $s_{eq}$  is apparently calculated using Eq. (11) [1] and the  $T_{\rm eq}$  data of Fig. 11(a) [1]; note that the slight, but noticeable, deviation from linearity (bump) in Fig. 11(a) [1] near  $a_{\text{eq}} = 12 \,\mu\text{m}$  is preserved in Fig. 11(b) [1].

The paper then reports a simple correlation for  $s_{\rm eq}$  as a function of  $a_{\rm eq}$  ( $\mu$ m) by a linear curve fit to the computational data of Fig. 11 [1]. This fitting gives the following equation:

$$s_{\text{eq}}(a_{\text{eq}}) = \varphi_{g,\text{eq}}(a_{\text{eq}}) - 1 = 0.01 \left( 1.7 \frac{a_{\text{eq}}}{10} - 0.5 \right),$$

$$10 < a_{\text{eq}} < 20 \,\mu\text{m}$$
(12)[1]

This type of curve-fitting was not necessary, and it misses important dependences on other parameters besides  $a_{\rm eq}$ . An equivalent fundamental relation to replace Eq. (12) [1] can be developed from existing theoretical developments, as shown below.

As discussed in Ref. [2], an equation that performs the same function as Eq. (12) [1] can readily be developed from Eq. (11) [1] by using Eq. (9) [1], the Clausius–Clapeyron relation, and Taylor series expansions. This has been described in the literature and is Eq. (61) in Ref. [2]. In the notation of Ref. [1], and with the Kelvin (surface tension) effect term omitted (which could easily be included but was not included in the analysis [1]), this equation would appear as

$$s_{\text{eq}}(a_{\text{eq}}) = \varphi_{g,\text{eq}}(a_{\text{eq}}) - 1 = \frac{H_p a_{\text{eq}} Q_a(a_{\text{eq}}) q}{4k}; \quad H_p = \frac{h_{\text{fg}}}{R_w T_{s,\text{eq}}^2}$$
(61)[2]

where q/4 is the collimated flux per unit surface area of droplet,  $h_{\rm fg}$  is the latent enthalpy, and  $R_w$  is the ideal-gas constant for water. Here,  $T_{s,\rm eq}$  is either droplet temperature  $T_{\rm eq}$  or gas temperature (here assumed to be  $T_s$ ) because Eq. (61) [2] is derived for near-saturation conditions, where the droplet and gas temperatures effectively merge into a single variable. (In practice, for levitated droplet conditions, the two temperatures are within 0.1– $0.7\,^{\circ}{\rm C}$  of each other, depending on radiant flux conditions.)

Equation (61) [2] applies to the equilibrium conditions of this experiment. When values for  $a_{\rm eq}$ ,  $Q_a$ , q,  $h_{\rm fg}$ , k, and  $T_{s,\rm eq}$  from Ref. [1] are substituted into Eq. (61) [2], the data of Fig. 11(b) [1] and Eq. (12) [1] are predicted to within the accuracy that the droplet absorption efficiency  $Q_a$  values can be read from Fig. 7 [1], as shown in Fig. 2(b). Equation (61) [2] is a theoretically based relation that describes the *nearly* linear relationship between  $s_{\rm eq}$  and  $a_{\rm eq}$  ("nearly," but not quite, linear because of  $Q_a(a_{\rm eq})$  for droplets not quite big enough to be opaque). It is the fundamental relation behind the curve-fit Eq. (12) [1] and the computational data of Fig. 11 [1].

It should be noted that to obtain accurate predictions using Eq. (61) [2], accurate input data should be used. If inaccurate input data (such as liquid–vapor phase-change enthalpy  $h_{\rm fg}(99\,^{\circ}{\rm C}) = 2260\,{\rm kJ/kg}$  [1]) were used, erroneous supersaturation would result. In the case of the calculations of Figs. 8(a) [1] and 11(b) [1], this inaccuracy in  $h_{\rm fg}$  did not introduce error because  $h_{\rm fg}$  was not used explicitly. This is because Eq. (11) [1] was used and accurate data for  $h_{\rm fg}$  (including temperature variation, i.e., Clausius–Clapeyron behavior) are implicitly built into the  $P_s$  correlation Eq. (7) [1].

## 3 Nonequilibrium (Transient) Conditions

Moving to nonequilibrium (transient) considerations, mist-size water droplets experiencing transient evolution (growth or evaporation) that is induced by a step change in radiative flux do so in a *quasi-steady* manner with respect to the droplet energy equation once a transient period on the order of 10 ms has passed [2,5]. This has been known since at least 1985 [5] and was reiterated in Ref. [2]. Yet, the authors [1] neglected to point this out with respect to the calculations and the results of Figs. 9 [1], 10 [1], and 12 [1] (t > 30 s). Instead of using the quasi-steady version of the droplet energy equation, Eq. (2) [1], the full transient energy equation was solved. The transient predictions of Figs. 9 [1] and

12 [1] for droplet radius and those of Fig. 10 [1] for droplet temperature can readily be predicted using the quasi-steady version of Eq. (2) [1], with  $\mathrm{d}T/\mathrm{d}t=0$ . This approach has been discussed in Ref. [2], along with use of the continuum (Fick's law) diffusion-mass-transfer approach, which is applicable under these conditions. The more complicated, noncontinuum Knudsen-layer approach of Ref. [1] is not necessary. The same results can be obtained by the continuum-diffusion, quasi-steady droplet energy approach if the same input properties are used, including the assumed  $h_{\rm fg}$  value (this is where the accuracy of  $h_{\rm fg}$  does matter).

The relevant quasi-steady droplet equations from Ref. [2] are Eq. (44a) [2] for droplet temperature and Eq. (44b) [2] for droplet growth rate. The droplet growth equation (differential form) with quasi-steady droplet energy for arbitrary ambient gas supersaturation s = (-1) and without Kelvin (surface tension) or Raoult's law (solute) effects is

$$\frac{da}{dt} = \frac{\frac{s(a)k}{aH_p} - \frac{Q_a(a)q}{4}}{\rho_w h_{fg} \left(1 + \frac{\Psi}{H_p}\right)} = \frac{s(a) - s_{eq}(a)}{\frac{aH_p \rho_w h_{fg}}{k} \left(1 + \frac{\Psi}{H_p}\right)};$$

$$\Psi = \frac{(1 - m_{1s})kR_w T_{s,eq}}{D_{w,a} h_{fg} P_s}$$
(44b)[2]

where  $D_{w,a}$  is the Fick's law binary diffusion coefficient or species diffusivity for water vapor in air. The value of  $D_{w,a}$  is taken to be  $3.2 \times 10^{-5}$  m<sup>2</sup>/s at 68 °C, 101 kPa, but for these conditions of radiant flux and temperature, the value of  $D_{w,a}$  does not have a strong influence on water-vapor transport rates because the parameter ratio  $\Psi/H_p$  is small (with  $h_{\rm fg}(99\,^{\circ}{\rm C}) = 2260\,{\rm kJ/kg}$  [1]):  $\Psi/H_p = 0.00149/0.0419 = 0.035 \ll 1$ . The water-vapor mass fraction at the droplet surface  $m_{1s}$  that appears in the  $\Psi$  parameter arises due to the convective or bulk mass flux transport of water at the droplet surface [4]. To make the dilute  $(m_{1s} \ll 1)$  theory of Refs. [2], [6], and [7] applicable to the nondilute conditions of the levitated droplets at the higher temperature conditions (e.g.,  $\sim$ 68 °C and  $m_{1s} \sim$  0.2), the  $\Psi$  parameter needs to be modified by including the multiplicative factor  $(1 - m_{1s})$ . The convective or bulk mass flux of water at the droplet surface is not negligible compared with the diffusive mass flux but is about 20% of the total flux for  $m_{1s} \sim 0.2$  [4].

The theoretical significance of the parameter ratio  $\Psi/H_p$  is discussed in Refs. [6] and [7]. This parameter ratio contains many thermophysical properties, but perhaps most importantly  $P_s(T)$ . Therefore, it can be thought of as a droplet volatility parameter, giving guidance about how irradiated (or radiatively cooled) water droplets would behave at different temperatures, or how different substances would behave compared to water (for example, how less volatile oil droplets would behave in space acting as liquid droplet radiators). The inverse parameter ratio,  $H_p/\Psi$ , can be interpreted as the relative increase in heating (or cooling) time scale of an assembly volatile (evaporating/condensing) droplets compared with nonvolatile droplets under the influence of a step change in radiant flux and can be approximated in terms of thermophysical properties as

$$\frac{H_p}{\Psi} = \left(\frac{h_{\rm fg}(T)}{R_w T}\right)^2 \frac{R_a}{C_{p,a}} \frac{P_s(T)}{P} \frac{\text{Le}}{(1 - m_{1s})}$$
(57)[7]

where  $C_{p,a}$  and  $R_a$  are specific heat and gas constant for air  $(C_{p,a}/R_a = 7/2)$ , P is pressure, and Le is Lewis number for air and water vapor (ratio of species over thermal diffusivities). The

parameter ratio  $\Psi/H_p$  also plays an important role in droplet growth rate when its magnitude is of order one (or larger), i.e., for lower-temperature conditions, as Eq. (44b) [2] shows. (Note that the notation  $H_p$  for the saturation pressure–temperature sensitivity parameter has been adopted here instead of H, which was used in Ref. [2], in order to make a distinction from the saturation density–temperature sensitivity parameter H, as delineated in Refs. [6] and [7].)

Assuming constant parameters, including assuming constant s and  $Q_a$ , a closed-form, algebraic solution for a(t) in the quasisteady case is possible and was published previously as follows:

$$\frac{a}{a_{\text{eq}}} - \frac{a_o}{a_{\text{eq}}} + \frac{s}{s_{\text{eq}}} \ln \left| \frac{a/a_{\text{eq}} - s/s_{\text{eq}}}{a_o/a_{\text{eq}} - s/s_{\text{eq}}} \right| = -\frac{t}{\tau};$$

$$\tau = \frac{a_{\text{eq}} \rho_w h_{\text{fg}} \left( 1 + \Psi/H_p \right)}{Q_a(q/4)}$$
(58)[2]

The predictions of this quasi-steady relation for a(t) can be compared with the predictions of the unsteady numerical computations in Ref. [1] if an assumption about the vapor supersaturation s is made. A common modeling assumption [6,7] is that every droplet, no matter its size, experiences the same ambient vapor supersaturation s. This assumption is demonstrated in the numerically computed results of Fig. 9 [1] with supersaturation assumed to be that of the final equilibrium state:  $s = s_{eq}(a_{eq})$ . In order to make quasisteady comparisons with Fig. 9 [1], this same assumption is made with  $s = s_{eq}(a_{eq})$  taken from Eq. (61) [2]. Calculations are made using Eq. (58) [2] for the same three droplet "variants" as in Fig. 9 [1], and the results are shown in Fig. 3 for t > 30 s, i.e., 30 s after the onset of broadband infrared irradiation, after which time quasi-steady conditions have been established in the droplet assembly. The experimental conditions are the same as those discussed above with Figs. 2(a) and 2(b) (Fig. 11 [1]):  $q = 5.58 \text{ kW/m}^2$  and  $T_s = 68.3 \,^{\circ}\text{C}$ . The same value for  $h_{\text{fg}}$ (2260 kJ/kg) is used for comparison purposes. The equilibrium value for droplet radius is  $18.8 \,\mu\text{m}$ . The predicted time histories for a(t) in Fig. 3 are essentially the same as those of Fig. 9 [1]. The latter calculation results are represented by discrete data points (squares) in Fig. 3. It should be emphasized that these discrete data points (squares) do not represent measurements of droplet radius evolution; measurements showed (Fig. 9 [1]) that nonequilibrium droplets actually evaporate or condense at slower rates than those calculated under the assumption of homogeneous supersaturation  $s = s_{eq}(a_{eq})$  in Fig. 3.

Droplet temperatures can be calculated using the quasi-steady droplet energy equation, Eq. (44a) [2], which, in the present notation with  $s = s_{eq}(a_{eq})$  from Eq. (61) [2], is

$$T - T_s = \frac{Q_a q \left(a_{eq} + a\Psi/H_p\right)}{4k\left(1 + \Psi/H_p\right)}$$
(44a)[2]

Droplet temperatures thus calculated are also shown in Fig. 3. The calculated equilibrium value for droplet temperature is 68.913 °C. The quasi-steady predictions of temperature in Fig. 3 differ from the unsteady predictions of Fig. 10 [1] by only a small fraction (a few hundredths) of a degree, which is inconsequential since the temperature variation is so slight as to be "not important," as noted in Ref. [1]. This slight difference may be attributable to unimportant differences between unsteady versus quasi-steady droplet energy approaches or kinetic versus continuum diffusion-mass-transfer approaches.

An important finding of Ref. [1] comes in the comparison between measurements of droplet-size evolution and predictions based on the assumption for supersaturation of  $s = s_{eq}(a_{eq})$  in

<sup>&</sup>lt;sup>5</sup>Due to the limitations of notation, the same symbol  $m_{Is}$ , which is here water-vapor mass fraction at the droplet surface (in the spherical droplet problem), is also used at the water layer surface (Cartesian Stefan flow problem). Fortunately, in practical numerical terms, the mass fraction is nearly constant from the water layer surface to a vapor location slightly above the surface, where resides a droplet, and from there to the droplet surface, so the common notation is allowed.

<sup>&</sup>lt;sup>6</sup>This seemingly long time scale, i.e., 30 s, for system quasi-steadiness compared with the shorter ∼10 ms time scales for droplet energy quasi-steadiness [1] and vapor supersaturation quasi-steadiness [6] is presumably due to the thermal inertia associated with heating the water layer and glass substrate.

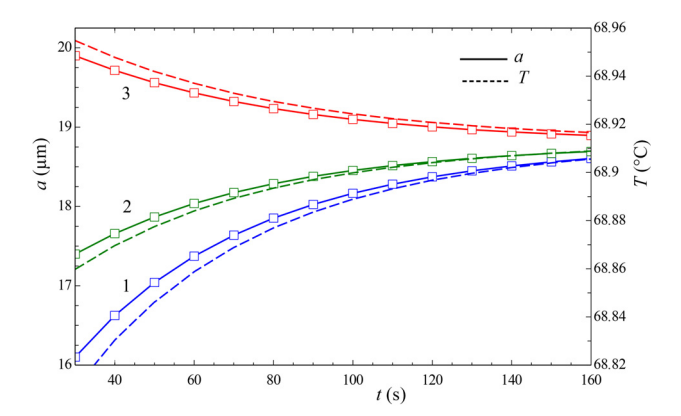


Fig. 3 Transient evolution of droplet radii a and temperatures T for three droplet variants of Figs. 9 and 10 [1] for a step change in infrared flux from q=0 to  $5.58\,\mathrm{kW/m^2}$  at time t=0 with a constant laser flux ( $T_s=68.3\,^\circ\mathrm{C}$ ,  $T_\mathrm{eq}=68.9\,^\circ\mathrm{C}$ ,  $s_\mathrm{eq}=2.56\%$ , and  $a_\mathrm{eq}=18.8\,\mu\mathrm{m}$ ) calculated using quasi-steady droplet Eqs. (58) [2] for a and (44a) [2] for T with  $s=s_\mathrm{eq}(a_\mathrm{eq})$  in Eq. (61) [2] and continuum (Fick's law) diffusion. The nearly identical calculations of a from Fig. 9 [1] are shown by discrete data points (squares).

Fig. 9 [1]. This comparison shows significant discrepancies for droplets that are initially appreciably larger or smaller than the equilibrium size, which led the authors to propose that the assumption of locally homogeneous supersaturation around all droplets of all sizes should be modified; see also Ref. [6] for this same suggestion. Figure 12 [1] presents improved calculations of the three transient variants of Fig. 9 [1], wherein the assumption of constant, uniform (spatially homogeneous)  $s = s_{eq}(a_{eq})$  is replaced by variable s in a linear, weighted combination of  $s_{eq}(a_{eq})$  and  $s_{eq}(a)$ 

$$s(a) = \gamma s_{eq}(a_{eq}) + (1 - \gamma) s_{eq}(a)$$
 (13)[1]

which incorporates the equilibrium supersaturation based on current droplet size:  $s_{\rm eq}(a)$ . Unsteady calculations using this modification were able to match measurements when the weighting parameter,  $\gamma(a) \sim 0.5 \pm 0.1$ , was varied slightly with droplet size. This same improvement in a(t) predictions can also be made using the quasi-steady droplet energy approach if the same adjustments to supersaturation are made, only instead of using Eq. (58) [2], which assumes constant s, Eq. (44b) [2] should be integrated numerically with varying s(a) and Eq. (61) [2] should be used for  $s_{\rm eq}(a_{\rm eq})$  and  $s_{\rm eq}(a)$  instead of Eq. (12) [1]. Another (different) rationale for how s(a) might be estimated for transient evolution (other than empirical curve-fitting) based on the vertical, flowinduced structure of s(y) is discussed in the Supplemental Materials on the ASME Digital Collection.

In summary to this point, a relatively simple, fundamentally based theoretical description of the radiation-stabilized, equilibrium, levitated droplet states described in Ref. [1] has been presented based on quasi-steady droplet energy and continuum transport. It has been shown how *a priori* prediction of equilibrium properties without the use of any measurements other than imposed radiant fluxes (i.e., *a priori* prediction of  $a_{\rm eq}$  and  $T_s$  based on input values of q and  $q_o$ ) can be done using previously published analytical results [2,3]. It has also been shown how *a priori* prediction of nonequilibrium, transient evolution (droplet evaporation and condensation) can be done provided an accurate description of nearby vapor supersaturation is available. Next, the stability of these equilibrium and nonequilibrium states is considered with the aid of classical, continuum heat- and mass-transfer theory.

## 4 Spalding Self-Similarity Model With Stefan Flow

First, consider the existence or stability of equilibrium states. When droplets are first formed by condensation in the vapor just

above the liquid surface without broadband infrared irradiation directly on the droplets, they grow in the supersaturated vapor environment until they are large enough to fall by gravity into the water layer. A stable equilibrium state with uniform droplet radius,  $a_{eq}$ , is only formed if a sufficient flux of infrared radiation from above is incident directly on the droplet array. The conditions of this equilibrium state and even its existence depend on the magnitudes of the radiant fluxes, as was demonstrated experimentally [1]. This existence versus nonexistence of states defines a stability boundary separating thermal conditions that allow equilibrium states to exist from those that do not allow equilibrium states to exist. This stability boundary is determined by the magnitudes of the two radiant fluxes in the experiment, broadbandinfrared and laser. Broadband infrared flux both heats the water layer and irradiates the droplets formed, while laser flux only heats the water layer (and is the primary source of heat into the water layer). Theoretical prediction or modeling of the levitated droplet equilibrium states, including their stability boundary, is possible using simple Stefan flow in the Spalding self-similarity model of heat and mass transfer [4].

The experimental observation that levitated equilibrium droplet clusters appear in stable, horizontal layers with nearly uniform-size distribution indicates that the upward air/water-vapor flow must also be relatively uniform horizontally in velocity, density, etc. This suggests that the upward vapor flow from the evaporating water surface can be approximated as a one-dimensional Stefan flow. Droplet radii  $a~(\sim 10~\mu \text{m})$  and corresponding upward vapor velocity necessary to levitate droplets ( $\sim 20~\text{mm/s}$ ) are such that  $0.01 < \text{Re}_a < 0.1$ , and therefore continuum Stokes flow applies to the vapor flow around the droplets (for a review of droplet flow regimes, see Fig. 9.5 of Ref. [8]). The Stokes flow relation between equilibrium droplet radius  $a_{\rm eq}$  (droplet radius at irradiated equilibrium, levitated, uniform-size condition) and upward vapor mass flux m (mass flux based on terminal fall velocity) is

$$a_{\rm eq} = \sqrt{\frac{9m\nu}{2g(\rho_w - \rho)}} \tag{1}$$

where  $\nu$  is the kinematic viscosity or momentum diffusivity of the air/water-vapor mixture, and the denominator contains the gravitational acceleration constant and the density difference between liquid water and vapor mixture. The relation between equilibrium supersaturation  $s_{\rm eq}$  and droplet radius for infrared flux q (also often used for transient, nonequilibrium states if it is assumed that all droplets experience the same equilibrium relation) from Ref. [2] was presented above

$$s_{\text{eq}}(a_{\text{eq}}) = \frac{H_p a_{\text{eq}} Q_a(a_{\text{eq}}) q}{4k}$$
 (61)[2]

Levitation of equilibrium droplets can occur when the Stefan-flow vapor supersaturation s is equal to the equilibrium value  $s_{eq}$ , as dictated by Eq. (61) [2]. This equality ( $s = s_{eq}$ ) defines an equilibrium state. To solve for s requires solving the Stefan flow with radiation included. Here, that is accomplished using the Spalding self-similarity model for heat and mass transfer. Relations for the Spalding self-similarity model with radiation included (but without condensation of water in the vapor-phase region above the vapor-liquid interface) can be found in Ref. [4]. In the Stefan model, a column of air and water-vapor mixture with horizontally uniform temperature, mass fractions, and velocity (slug flow) flows vertically upward above a layer of evaporating water that is heated by collimated broadband infrared flux q incident from above at 45 deg and collimated laser flux  $q_o$  normally incident from below. The vapor column has vertical height L with conditions at the bottom of the column, i.e., at the water surface in the vapor phase, designated by subscript-s, and conditions at the top of the column, the ambient environmental conditions, designated

Table 2 Modeling parameters and results for equilibrium properties of levitated droplets based on Stefan flow and Spalding selfsimilarity heat and mass transfer theory

		$q (kW/m^2)$	$q_o$ (kW/m <sup>2</sup> )	L  (mm)	$T_e$ (°C)	$\varphi_e$	$T_s$ (°C)	$\Delta T_s/T_{s0}$ (%)	$a_{\mathrm{eq}} \left( \mu \mathrm{m} \right)$
1	(a) <sup>a</sup>	0	50	0.25	25	0.75	63.0 (62.9)		
2	(b)	5.58	0	2.5	25	0.75	59		
3	(c) <sup>b</sup>	5.58	50	0.12	57	1	66.5 (66.7)	5.6 (6.0)	13.3 (13.5)
4	$(c)^{b}$	5.58	100	0.09	58	1	70.1 (69.3)		18.5 (18.8)
5	(c)	5.58	30	0.14	56	1	64.7		None (none)
6	(a) <sup>a</sup>	0	30	0.19	25	0.75	49.6 (48.0)		
7	(b)	3.85	0	1.9	25	0.75	48.1		
8	(c) <sup>b</sup>	3.85	30	0.075	47.8	1	54 (52.3)	8.9 (9.0)	9.92 (9.95)
9	(a) <sup>a</sup>	0	10	0.13	25	0.75	31.8		
10	(b)	1.55	0	1.7	25	0.75	35		
11	(c) <sup>b</sup>	1.55	10	0.042	35	1	37.4	17.6 (17.5)	5.4 (5.5)

<sup>&</sup>lt;sup>a</sup>When q = 0,  $T_s = T_{s0}$ .

by subscript-*e*. Mass fraction of water vapor is  $m_1$ , and vapor mixture enthalpy is h. Assuming constant product of density  $\rho$  and diffusivity (species  $D_{w,a}$  or thermal  $\alpha = k/\rho C_p$ ), the solution for surface temperature and upward mass flux m is embodied in the following equations:

$$m = \frac{\rho D_{w,a}}{L} \ln \left[ \frac{1 - m_{1e}}{1 - m_{1s}} \right] \tag{2}$$

$$m = \frac{\rho \alpha}{L} \ln \left[ 1 + \frac{h_s - h_e}{q_{r,s}/m + h_o - h_s} \right]; \quad q_{r,s} = q \cos 45 \deg + q_o$$
 (3)

The sign convention of the radiation flux  $q_{r,s}$  is positive down (i.e., to the water) here and in Refs. [2] and [4], which is the reverse of the sign convention of some later papers [6,7]. The enthalpy  $h_o$  is that of the water fed to the evaporative slide. The combination of Eqs. (2) and (3) with m eliminated can be solved for water surface temperature  $T_s$ . The enthalpy and mass-fraction profiles in the vapor column from the surface (s), y = 0, up to the ambient environment (e), y = L, are then given by

$$\frac{h(y) - h_s}{h_e - h_s} = \frac{1 - \exp\left[my/\rho\alpha\right]}{1 - \exp\left[mL/\rho\alpha\right]} \tag{4}$$

$$\frac{m_1(y) - m_{1s}}{m_{1e} - m_{1s}} = \frac{1 - \exp\left[my/\rho D_{w,a}\right]}{1 - \exp\left[mL/\rho D_{w,a}\right]}$$
(5)

The Stefan-flow supersaturation profile is obtained from the definition of supersaturation and the temperature and water-vapor mass-fraction profiles, where the relation between mixture enthalpy and temperature is the usual one for an ideal-gas mixture of air and water vapor and the temperature dependences of air and water-vapor enthalpies are from standard, ideal-gas polynomial fits

The approach for applying the Stefan-flow analysis to the experimental measurements is illustrated in Fig. 1. The two different radiation sources, laser and broadband-infrared, which have spot diameters of 1 mm and 1 cm, respectively, produce two distinct Stefan flows. An inner Stefan flow is produced by the laser heating. An outer Stefan flow is produced by the broadband infrared flux. The outer flow creates the ambient condition (y = L or estate boundary condition) for the inner flow. Three situations with different irradiation conditions are depicted in Fig. 1: (a) with only laser heating from below (no infrared flux q from above); (b) with only infrared flux from above (no laser flux q from below); and (c) with both infrared flux from above and laser flux from below, i.e., the experimental condition that produced equilibrium levitated droplets within the inner flow. The first case (a) is necessary because it produces the surface temperature  $T_{s0}$  without

broadband infrared irradiation as reported in Ref. [1]. The second case (b) is necessary because it produces the y=L boundary conditions for the inner Stefan flow. The location of the upper boundary condition y=L is different for each of the three situations, and the L value is a modeling parameter that is guided by the laser beam diameter (1 mm), the broadband irradiated spot diameter (1 cm), and the radiative fluxes, which determine the evaporative mass flux. Ultimately, the value of L is chosen to match measured surface temperatures with  $(T_s)$  and without  $(T_{s0})$  broadband radiation. The ambient laboratory conditions were assumed to be  $25\,^{\circ}\text{C}$  and 75% relative humidity (the latter choice is arbitrary and rather inconsequential); the temperature of the water fed to the irradiated evaporation slide was taken to be  $15\,^{\circ}\text{C}$  based on Ref. [1]; this temperature determines the enthalpy  $h_o$  in Eq. (3).

The first case considered with Stefan-flow modeling is the experiment with conditions near the stability boundary shown in Table 1 column 6 having broadband flux  $q = 5.58 \text{ kW/m}^2$ . The modeling conditions for configuration (c) of this case are shown in line 3 of Table 2. The value of absorbed laser flux that was found to match experimental measurements of  $T_s$  (66.7 °C) and  $T_{s0}$  (62.9 °C) reasonably well was  $q_o = 50 \,\mathrm{kW/m^2}$ . The laser-only experimental configuration (a) was modeled using the parameters shown in line 1 of Table 2. The effective Stefan column height was L = 0.25 mm, or one quarter of the laser beam diameter. The resulting surface temperature of 63.0 °C matches the measured  $T_{s0}$ value of 62.9 °C reasonably well. The broadband-only configuration (b) was modeled with parameters shown in line 2. The effective Stefan column height was L = 2.5 mm, or one quarter of the broadband beam diameter. The calculated temperature profile decreased from 59°C at the surface to 57°C at a height of  $0.12 \,\mathrm{mm}$ , which was the value of L for the (c) configuration in line 3; therefore, 57 °C was used as the effective  $T_e$  value for case (c) on line 3 (relative humidity at that location was effectively 100% or supersaturation of zero). The configuration (c) calculated values for  $T_s$ ,  $\Delta T_s/T_{s0}$ , and  $a_{\rm eq}$  of 66.5 °C, 5.6%, and 13.3  $\mu \rm m$  match the measured values (66.7 °C, 6.0%, and 13.5  $\mu$ m) reasonably well. The calculated temperature profile for configuration (c) is shown in Fig. 4 as the solid curve with circle symbols. The corresponding water-vapor mass-fraction profile is shown as the dashed curve with circle symbols. The mass fraction drops from about 0.18 at the surface to 0.11 at the top of the Stefan layer.

Since formation of equilibrium droplets depends on the magnitude of vapor-phase supersaturation s relative to a radiation-stabilized equilibrium value  $s_{\rm eq}$  from Eq. (61) [2], the next parameter to consider is flow supersaturation. The supersaturation profile in the vapor phase is, by its definition, a combination of the temperature and mass-fraction profiles. Both temperature and mass fraction decrease with distance above the surface, as shown in Figs. 5 and 6. Decreasing temperature tends to produce an increase in supersaturation. Decreasing mass fraction tends to

<sup>&</sup>lt;sup>b</sup>Quantities in parentheses are from Fig. 4 [1] or Table 1 [1] except for line 4, which are from the text of Sec. 5.3 [1].

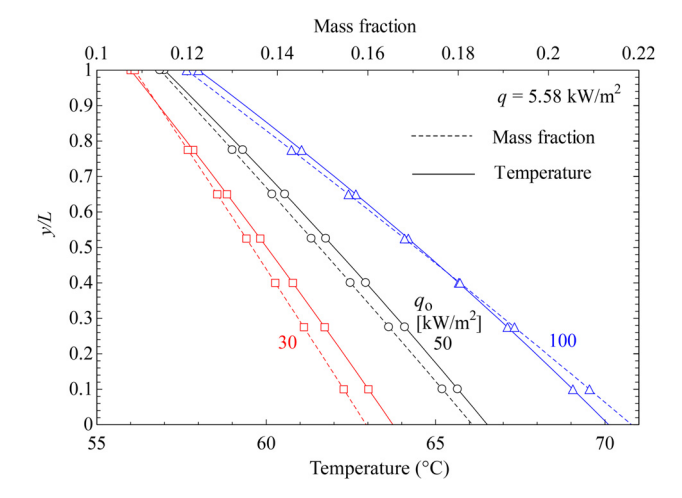


Fig. 4 Spalding/Stefan model temperature and water-vapor mass-fraction profile predictions for cases on Table 2 lines 3–5

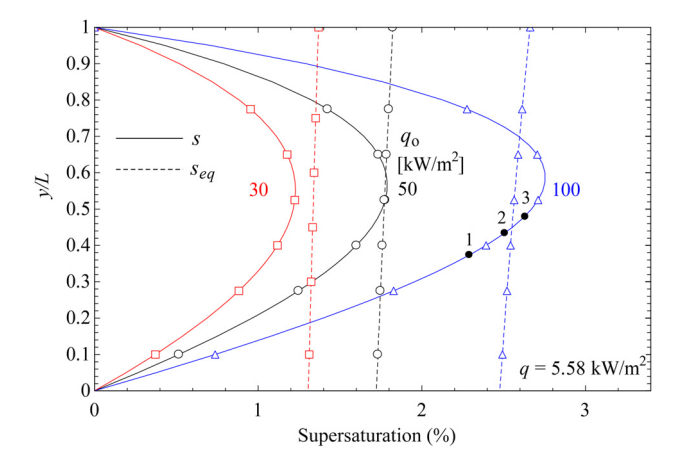


Fig. 5 Spalding/Stefan model supersaturation profile predictions for cases on Table 2 lines 3–5; solid dots correspond to approximate locations of nonequilibrium droplets or variants 1–3 of Fig. 3 at  $t=30\,\mathrm{s}$ 

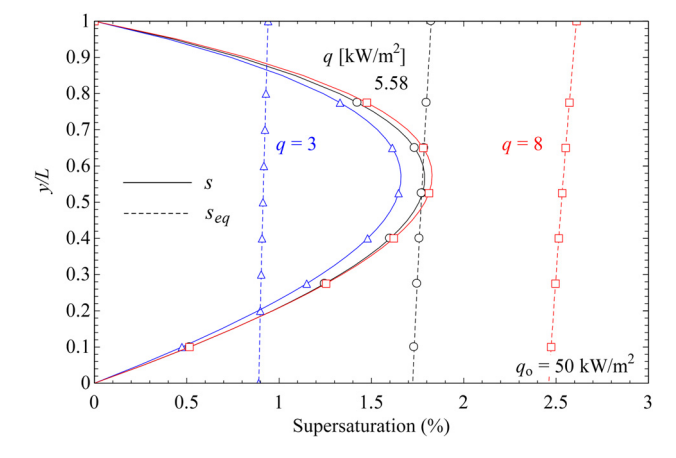


Fig. 6 Spalding/Stefan model supersaturation profile predictions for case on Table 2 line 3 with variations in broadband infrared flux q

produce a decrease in supersaturation. When the effect of both profiles is combined, the calculations indicate, as shown in Fig. 5, that just above the surface the temperature effect is stronger and supersaturation increases, reaching a maximum at about 1.8% at a

relative height  $y/L \sim 0.6$ , as shown by the curve in Fig. 5 with circle symbols. It happens that the  $s_{\rm eq}$  curve calculated by Eq. (61) [2], shown by the nearly vertical dashed line with circle symbols, reaches this same value, 1.8%, at the same location. This situation illustrates conditions that are on the stability boundary.

To illustrate the effect of increasing laser flux above the stability-boundary value of  $50 \text{ kW/m}^2$  (for  $q = 5.58 \text{ kW/m}^2$ ), consider next the case with parameters shown in line 4 of Table 2 and  $q_o$  increased to  $100 \,\mathrm{kW/m^2}$ . This situation corresponds to a case that was discussed above along with discussion of Figs. 2, 3, and 11 [1] and in Sec. 5.3 of Ref. [1]. This case, at equilibrium, was deemed to be relatively far from the stability boundary and produced a relatively large equilibrium levitated droplet radius of 18.8  $\mu$ m with a surface temperature of 69.3 °C (see also Table 1 column 7). The calculated temperature and mass-fraction profiles for this case are shown in Fig. 4 by the curves with triangle symbols, and the supersaturation profile is shown in Fig. 5 by the curve with triangle symbols. At this higher laser flux of  $q_o = 100 \,\mathrm{kW/m^2}$ , the supersaturation curve in Fig. 5 has shifted relative to the  $s_{eq}$  curve such that there are two locations where  $s = s_{eq}$  and equilibrium droplets could exist,  $y/L \sim 0.45$  or 0.7. This case is thus somewhat removed from the stability boundary. The higher evaporation mass flux from the horizontal water surface produced by the higher laser flux is able to levitate larger droplets compared with the previous case. The calculated values for  $T_s$  and  $a_{eq}$  of 70.1 °C and 18.5  $\mu$ m match the measured values (69.3 °C and 18.8  $\mu$ m) reasonably well. The supersaturation value, though it is difficult to measure and was not reported in Ref. [1], was calculated to be a plausible value of 2.5% to 2.6%, as shown in Fig. 5, consistent with the calculated value of 2.56% reported in Fig. 11(b) [1]. The question of which of the two solutions depicted in Fig. 5 for this case is the more likely one is a matter of stability considerations and is discussed in the Supplemental Materials on the ASME Digital Collection.

To illustrate the effect of decreasing laser flux below the stability-boundary value of  $50 \, \mathrm{kW/m^2}$  (for  $q = 5.58 \, \mathrm{kW/m^2}$ ), consider next the case with parameters shown in line 5 of Table 2, with  $q_o$  decreased to  $30 \, \mathrm{kW/m^2}$ . The temperature and massfraction profiles for this case are shown in Fig. 4 by the curves with square symbols, and the supersaturation profile is shown in Fig. 5 by the curve with square symbols. At this laser flux, the supersaturation curve of Fig. 5 has shifted relative to the  $s_{\rm eq}$  curve such that there are no y/L locations where equilibrium droplets could exist; the s (solid line) and  $s_{\rm eq}$  (dashed line) curves in Fig. 5 do not intersect

The key to the existence of equilibrium states is that Stefan flow that is constrained to be saturated at the water surface (by thermodynamic equilibrium) and saturated at the  $y\!=\!L$  location (by, in this experiment, an outer Stefan flow induced by the broadband irradiation) will have a supersaturation profile with a quadratic behavior; there will be a local maximum in s value at some intermediate location above the surface,  $0 \le y \le L$ , as seen in Fig. 5. On the other hand, the equilibrium supersaturation, according to Eqs. (61) [2] and (1), is nearly constant;  $s_{\rm eq}$  appears as a nearly vertical straight line on Fig. 5 with a slight nonvertical slope due to temperature dependence in the  $H_p$  parameter. Solutions to  $s\!=\!s_{\rm eq}$  can happen at zero, one, or two y locations, depending on the magnitudes of q and  $q_o$ .

The existence or nonexistence of equilibrium droplet solutions as a function of q and  $q_o$  can also be illustrated by fixing laser flux  $q_o$  and varying broadband infrared flux q, as shown in Fig. 6. In Fig. 6, the laser flux is fixed at  $q_o = 50 \,\mathrm{kW/m^2}$ . The previous case with broadband flux of  $q = 5.58 \,\mathrm{kW/m^2}$  is shown again by curves with circle symbols. This is the solution with just one intersection point between s and  $s_{\rm eq}$  that is just on the stability boundary. Now because laser flux  $q_o$  is fixed, broadband infrared flux q must be decreased to achieve two intersection points between s and  $s_{\rm eq}$ . This is illustrated by the curve for  $q = 3 \,\mathrm{kW/m^2}$  with triangle symbols. And to achieve no intersection points, q must be increased, as illustrated by the curve for  $q = 8 \,\mathrm{kW/m^2}$  with square symbols.

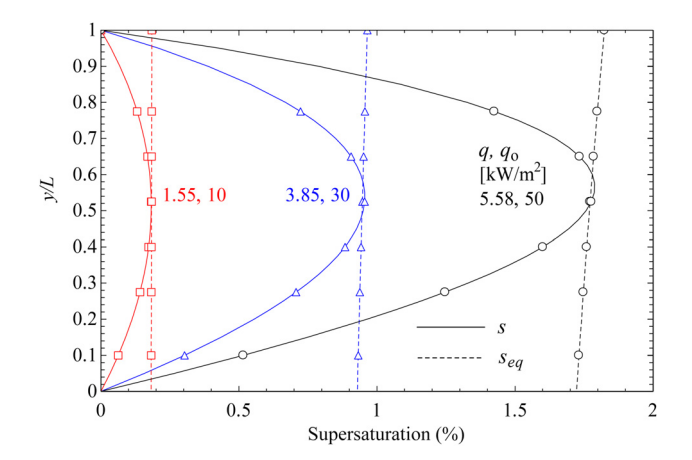


Fig. 7 Spalding/Stefan model supersaturation profile predictions for three cases on stability boundary from Table 2 lines 3, 8, and 11

It should be noted that unlike in Fig. 5 with varying  $q_o$ , the calculations for Fig. 6 were not tuned to be more realistic by adjusting L. The trends, however, are the same with a fixed L (0.12 mm); the point of Fig. 6 is to illustrate the role reversal of q and  $q_o$  when the latter is fixed.

With the trends of Figs. 5 and 6 established, it is possible to seek other solutions or cases on the stability boundary. The next case chosen is column 3 of Table 1 having broadband flux  $q = 3.85 \text{ kW/m}^2$ . The modeling conditions for configurations (a–c) of this case are shown in lines 6-8 of Table 2. The value of absorbed laser flux that was found to match experimental measurements for  $T_s$  and  $T_{s0}$  reasonably well was  $q_o = 30 \,\text{kW/m}^2$ . The laser-only experimental configuration (a) was modeled using the parameters shown in line 6 of Table 2. The effective Stefan column height was L = 0.19 mm. The resulting surface temperature of 49.6 °C matches the measured  $T_{s0}$  value of 48.0 °C reasonably well. The broadband-only configuration (b) was modeled with parameters shown in line 7. The effective Stefan column height was  $L = 1.9 \,\mathrm{mm}$ . The calculated temperature profile decreased from 48.1 °C at the surface to 47.8 °C at a height of 0.075 mm, which was the value of L for the (c) configuration in line 8; therefore,  $47.8\,^{\circ}\text{C}$  was used as the effective  $T_e$  value for case (c) on line 8. The configuration (c) calculated values for  $T_s$ ,  $\Delta T_s/T_{s0}$ , and  $a_{\rm eq}$  of 54 °C, 8.9%, and 9.92  $\mu{\rm m}$  match the measured values (52.3 °C, 9.0%, and 9.95  $\mu{\rm m}$ ) reasonably well. The supersaturation profile for this case is shown in Fig. 7, along with the previous case for  $q=5.58\,{\rm kW/m^2}$  and  $q_o=50\,{\rm kW/m^2}$ .

A third case on the stability boundary can be obtained from Fig. 4 [1] (see also column 1 of Table 1) and has an equilibrium droplet radius of 5.5  $\mu \rm m$  with a relative surface temperature increase of 17.5%. This case was matched by Stefan-flow modeling with a broadband flux of  $q=1.55\,\rm kW/m^2$  and a laser flux of  $q_o=10\,\rm kW/m^2$ . Other modeling conditions for this case are shown in lines 9–11 of Table 2. The configuration (c) calculated values for  $\Delta T_s/T_{s0}$  and  $a_{\rm eq}$  of 17.6% and 5.4  $\mu \rm m$  match the reported measured values (17.5% and 5.5  $\mu \rm m$ ) reasonably well. The supersaturation profile for this case is also shown in Fig. 7, along with the other cases that are on, or very nearly on, the stability boundary, having just one intersection point between s and  $s_{\rm eq}$ . With the stability boundary trends of Figs. 5–7 in terms of

With the stability boundary trends of Figs. 5–7 in terms of supersaturation profiles established, it is possible to make stability maps in terms of other variables, such as the two independent radiation fluxes q and  $q_o$ . Figure 8(a) shows the simplest version of such a plot with broadband infrared flux q versus laser flux  $q_o$  and using the three experimental cases illustrated in Fig. 7. The lower right portion of Fig. 8(a) gives values of q and  $q_o$  for which equilibrium levitated droplet solutions exist, i.e., for which there are one or two intersections between the s and  $s_{\rm eq}$  curves. Figure 8(b) shows the values of equilibrium droplet radius  $a_{\rm eq}$  on the stability boundary based on these three cases, with the understanding that both q and  $q_o$  vary along the curve but only one can be plotted on the horizontal axis as an independent variable.

Other stability maps can be generated by different choices of plot variables. To aid in understanding Fig. 4 [1], a modified stability map, Fig. 9(a), was created by changing the vertical axis of Fig. 8(a) from q to  $q/q_o$ . As a result, the slope of the boundary changes signs, and the region of stability or existence of equilibrium levitated droplet solutions shifts to the upper right region. Figure 8(a) is similar in character to Fig. 4(a) [1], but, whereas Fig. 4(a) [1] uses dependent variables ( $T_s$  and  $T_{s0}$ ), Fig. 8(a) uses independent variables ( $T_s$  and  $T_{s0}$ ), Fig. 8(a) uses independent-variable based) version of Fig. 4(b) [1] for equilibrium droplet radius  $T_{s0}$ 0 on the stability boundary versus  $T_s/T_{s0}$ 0 can be generated by changing the horizontal axis of Fig. 8(b) from  $T_s$ 0 to  $T_s$ 1 as shown in Fig. 9(b).

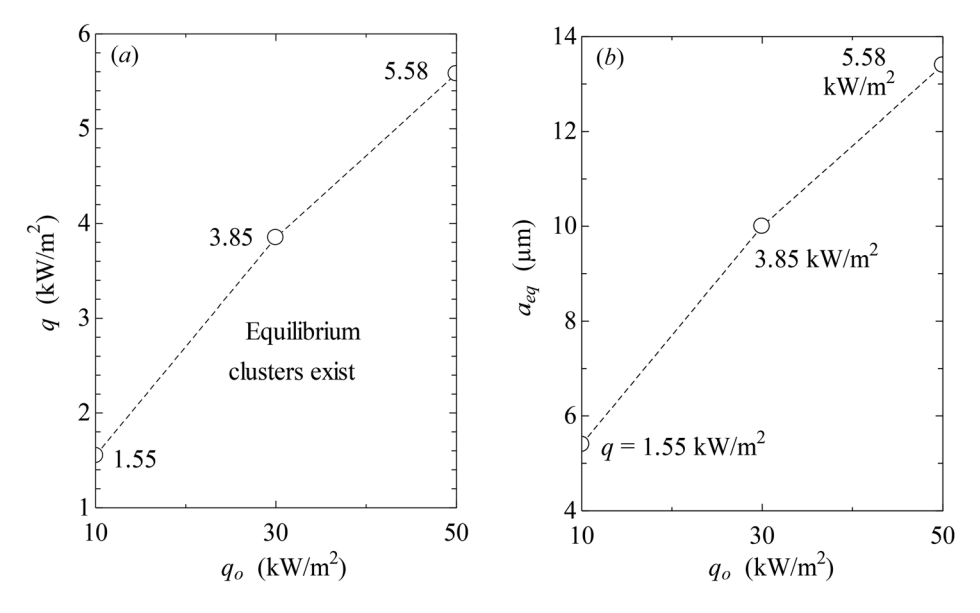


Fig. 8 (a) Spalding/Stefan model stability boundary predictions based on three cases from Table 2 lines 3, 8, and 11; and (b) corresponding equilibrium droplet radius predictions

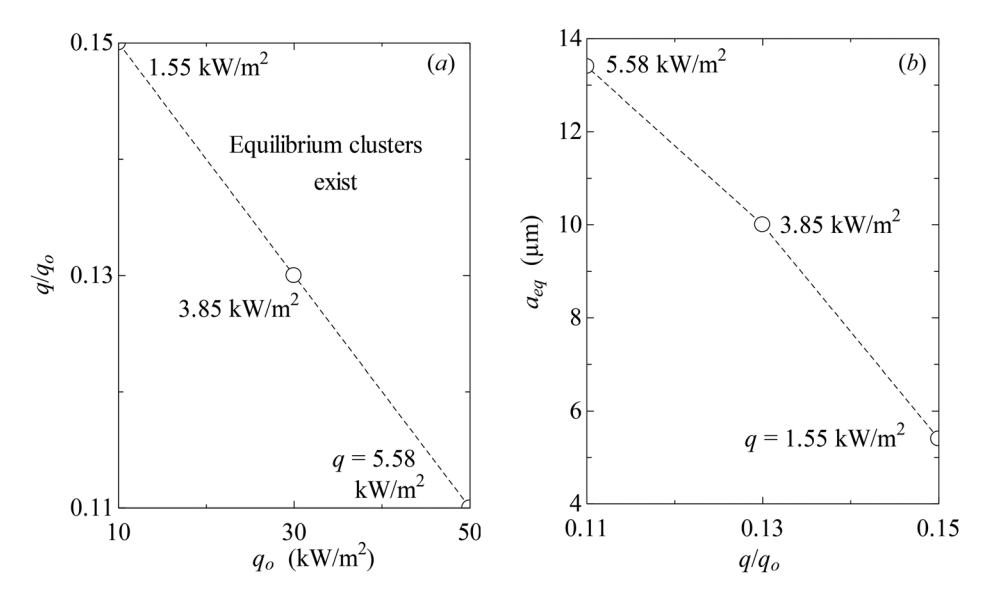


Fig. 9 (a) Variation of Fig. 8(a) intended to correspond to Fig. 4(a) [1] and (b) variation of Fig. 8(b) intended to correspond to Fig. 4(b) [1]

### 5 Discussion

An interesting aspect of the levitation experiments not discussed in Ref. [1] is that droplets with radii different than  $a_{eq}$ were able to be stably levitated even though (nonevaporating) noncondensing) droplets of different radii would experience different drag force and would therefore have different fall velocities than the equilibrium Stefan-flow velocity. The only apparent way to explain this observation is that evaporation and condensation mass transfer must affect droplet drag force. In these levitation experiments, the effect of mass transfer on drag force must have been such as to make the drag on smaller ( $a < a_{eq}$ ), condensing droplets, which otherwise would have been carried up and away by the Stefan flow, be less than that on a noncondensing droplet of the same radius, so that the fall velocities were the same. Similarly, the effect of mass transfer must have been so as to make the drag force on larger  $(a > a_{eq})$ , evaporating droplets, which otherwise would have fallen to the water surface, be greater than that on a nonevaporating droplet of the same radius, so that the fall velocities would again be the same. This effect of mass transfer on drag (i.e., condensation reducing drag; evaporation increasing drag) is opposite what has been reported from conventional experimental and computational studies for droplets in the "low" Reynolds number range without external irradiation [9]; however, apparently it is the case here with significant external irradiation incident from above (downstream of) the droplets. For discussion of why the effect of mass transfer on drag in asymmetrically irradiated, nonequilibrium (condensing or evaporating) levitated droplets might be opposite the more commonly observed effect in nonirradiated droplets (which has to do with the relative importance of pressure versus shear-stress drag), see Supplemental Materials on the ASME Digital Collection.

## 6 Summary

This paper describes modeling of radiation-stabilized, water droplets levitated by an upward vapor flow, about which experimental results have recently been reported [1]. Results show how modeling the upward vapor flow as Stefan flow in the framework of Spalding's self-similarity theory of heat and mass transfer can describe the droplet equilibrium states, including stability conditions. Droplets are levitated in stable equilibrium states when the radiative heat gained by the droplets is balanced by the conductive heat lost to the vapor surroundings and the virtual evaporative

mass flux that would be induced by the radiation absorption is balanced by the virtual condensation mass flux that would be induced by the surrounding vapor's supersaturation. At these stable equilibrium conditions, the vapor supersaturation s and the theoretical equilibrium supersaturation s agiven by previously published Eq. (61) [2], are equal. For most radiant fluxes, Stefan-flow modeling predicts either two or no vertical locations above the surface where this equality can exist. This is because s has a quadratic-like behavior as a function of height above the water surface, whereas s is nearly constant with height above the surface. For certain combinations of broadband infrared (droplet-irradiating) flux and water-heating (laser) radiation, there is just one intersection or solution of equality between s and s eq; this set of conditions defines the stability boundary for the existence of equilibrium levitated droplets.

This work also shows how modeling results that were obtained in Ref. [1] by empirical curve-fitting and numerical computation and described as new results could have been readily calculated with existing simple, analytically obtained algebraic equations that were available in the literature. The algebraic expression for equilibrium supersaturation  $s_{eq}$  as a function of droplet radius, absorbed radiant flux, and thermophysical properties that was found analytically and published as Eq. (61) in Ref. [2] predicts the empirically/numerically found correlation, Eq. (12) [1]. A simple algebraic solution for transient evolution of droplet radius induced by a step change in radiant flux as a function of absorbed radiant flux and thermophysical properties that was found analytically and published as Eq. (58) in Ref. [2] predicts the numerically computed results for transient droplet evolution in Ref. [1]. The basis of these simple analytical results is the quasi-steady droplet energy condition. This paper demonstrates that the quasi-steady droplet energy condition is applicable and useful in analyzing and modeling these phenomena, along with continuum diffusion-mass-transfer theory. Knudsen-layer modeling appears not to be necessary.

In summary, previously published analytical results are applied to radiation-stabilized, levitated water droplet experimental conditions and measurements and shown to predict the same results as numerical computations, but with the benefits of greater computational efficiency, more complete theoretical background, less empiricism or curve-fitting, and less brute-force numerical computation. Moreover, a Stefan/Spalding heat and mass transfer model is developed that is able to "predict" (with an empirical vapor-column height parameter) the equilibrium states, including droplet radius, as a function of imposed radiant fluxes, as well as stability conditions, i.e., existence or nonexistence of equilibrium

states. Stefan-flow modeling revealed that temperature change between the horizontal water surface and the levitated droplet location is sufficiently large (up to 5 °C) that the assumption of no temperature change made in equilibrium calculations should be corrected. A reversal has also been postulated of the usual effect of mass transfer on droplet drag when levitated droplets are irradiated asymmetrically from above by sufficient infrared flux.

These results underscore the importance of radiation in influencing the evaporation and condensation dynamics of water mists and clouds. The Spalding model, augmented with theoretical considerations from Refs. [2–4], [6], and [7], provides an appropriate theoretical treatment that could be used to describe these phenomena in more complex simulations, such as cloud-dynamics or general two-phase flow modeling.

## Acknowledgment

The first part of this paper (Secs. 1–3 and Figs. 2 and 3) having to do with errors and oversights in Ref. [1] was submitted as a Comment to the *Int. J. Heat Mass Transfer* in December 2020, but publication of the Comment was declined without addressing or acknowledging these errors and oversights. This work was enabled by support from the H. G. Soo Professorship.

#### References

- [1] Dombrovsky, L. A., Fedorets, A. A., Levashov, V. Y., Kryukov, A. P., Bormashenko, E., and Nosonovsky, M., 2020, "Stable Cluster of Identical Water Droplets Formed Under the Infrared Irradiation: Experimental Study and Theoretical Modeling," Int. J. Heat Mass Transfer, 161, p. 120255.
- [2] Brewster, M. Q., 2015, "Evaporation and Condensation of Water Mist/ Cloud Droplets With Thermal Radiation," Int. J. Heat Mass Transfer, 88, pp. 695–712.
- [3] Brewster, M. Q., 2016, "Corrigendum to 'Evaporation and Condensation of Water Mist/Cloud Droplets With Thermal Radiation' [International Journal of Heat and Mass Transfer 88 (2015) 695-712]," Int. J. Heat Mass Transfer, 96, pp. 703–704.
- [4] Brewster, M. Q., 2017, "Water Evaporation and Condensation in Air With Radiation: The Self-Similar Spalding Model," ASME J. Heat Transfer-Trans. ASME, 139, p. 081501.
- [5] Davies, R., 1985, "Response of Cloud Supersaturation to Radiative Forcing," J. Atmos. Sci., 42(24), pp. 2820–2825.
- [6] Brewster, M. Q., Li, X., Roman, K. K., McNichols, E. O., and Rood, M. J., 2020, "Radiation-Induced Condensational Growth and Cooling of Cloud-Sized Mist Droplets," J. Atmos. Sci., 77(10), pp. 3585–3600.
- [7] Brewster, M., and Li, X., 2021, "Analysis of Radiation-Induced Cooling and Growth of Cloud-Sized Mist Droplets," Int. J. Heat Mass Transfer, 166, p. 120674.
- [8] Lamb, D., and Verlinde, J., 2011, Physics and Chemistry of Clouds, Cambridge University Press, Cambridge, UK, Chap. 9.
- [9] Dukowicz, J. K., 1984, "Drag of Evaporating or Condensing Droplets in Low Reynolds Number Flow," Phys. Fluids, 27(6), pp. 1351–1358.